



PERGAMON

Neural Networks 12 (1999) 499–511

Neural
Networks

Contributed article

A neural network for enhancing boundaries and surfaces in synthetic aperture radar images

Ennio Mingolla, William Ross, Stephen Grossberg*

Department of Cognitive and Neural Systems and Center for Adaptive Systems, Boston University, 677 Beacon Street, Boston, MA 02215, USA

Received 27 January 1998; received in revised form and accepted 22 October 1998

Abstract

A neural network system for boundary segmentation and surface representation, inspired by a new local-circuit model of visual processing in the cerebral cortex, is used to enhance images of range data gathered by a synthetic aperture radar (SAR) sensor. Boundary segmentation is accomplished by an improved Boundary Contour System (BCS) model which completes coherent boundaries that retain their sensitivity to image contrasts and locations. A Feature Contour System (FCS) model compensates for local contrast variations and uses the compensated signals to diffusively fill-in surface regions within the BCS boundaries. Image noise pixels that are not supported by BCS boundaries are hereby eliminated. More generally, BCS/FCS processing normalizes input dynamic range, reduces noise, and enhances contrasts between surface regions. BCS/FCS processing hereby makes structures such as motor vehicles, roads, and buildings more salient to human observers than in original imagery. The new BCS model improves image enhancement with significant reductions in processing time and complexity over previous BCS applications. The new system also outperforms several established techniques for image enhancement. © 1999 Elsevier Science Ltd. All rights reserved.

Keywords: Synthetic aperture radar; Neural network; Image enhancement; Boundary segmentation; Diffusion

1. Introduction

Synthetic aperture radar (SAR) sensors can produce range imagery of high spatial resolution under difficult weather conditions (Munsen et al., 1983; Munsen and Visentin, 1989) but the image data can be difficult to interpret by human observers for several reasons. First, the sensors respond over a dynamic range of five orders of magnitude, thereby demanding some type of nonlinear compression merely for an image to be represented for viewing on a typical computer monitor (see Fig. 1(a)). Second, multiplicative noise or image speckle results from the coherent processing of radar signals and degrades the appearance of features in the image (see Fig. 1(b)).

To date, simple techniques for image display and enhancement have been used to process SAR data. Logarithmic scaling of sensor values has been used to compress sensor data to allow display on 8-bit video monitors, as in Fig. 1(b). This technique tends to reduce local image contrasts in order to provide display capability over the full range of possible sensor values.

Simple statistical models for signal and noise have also

been used to reduce speckle. These models typically sacrifice a portion of the signal in order to eliminate noise (Lee, 1983). Iterative smoothing techniques have also been used. These techniques suffer from insensitivity to scenic structure and tend to blur the boundaries between surfaces, especially if they are iterated too often. The number of iterations needed for the best results may depend upon the image being processed. This limitation is illustrated for SAR processing through adaptive averaging with a sigma filter (Lee, 1983) and a geometric filter (Crimmins, 1985) by Grossberg et al. (1995).

Our approach further develops the use of surface contrast enhancement, normalization, and diffusive filling-in between form-sensitive boundary signals as a technique for SAR image enhancement, as described by Grossberg et al. (1995). Our algorithm capitalizes on the structure-sensitive operations of a neural model of early visual processing in order to enhance the appearance of scenic surfaces based on information distributed across large regions of the image.

The boundary processing that we describe in this article is improved from prior published versions by incorporation of stages that more closely model recently discovered cortical mechanisms for enhancing the salience of globally consistent form information in the image, by strengthening,

* Corresponding author. Tel.: (617) 353-7857; fax: (617) 353-7755.

E-mail address: steve@cns.bu.edu (S. Grossberg)

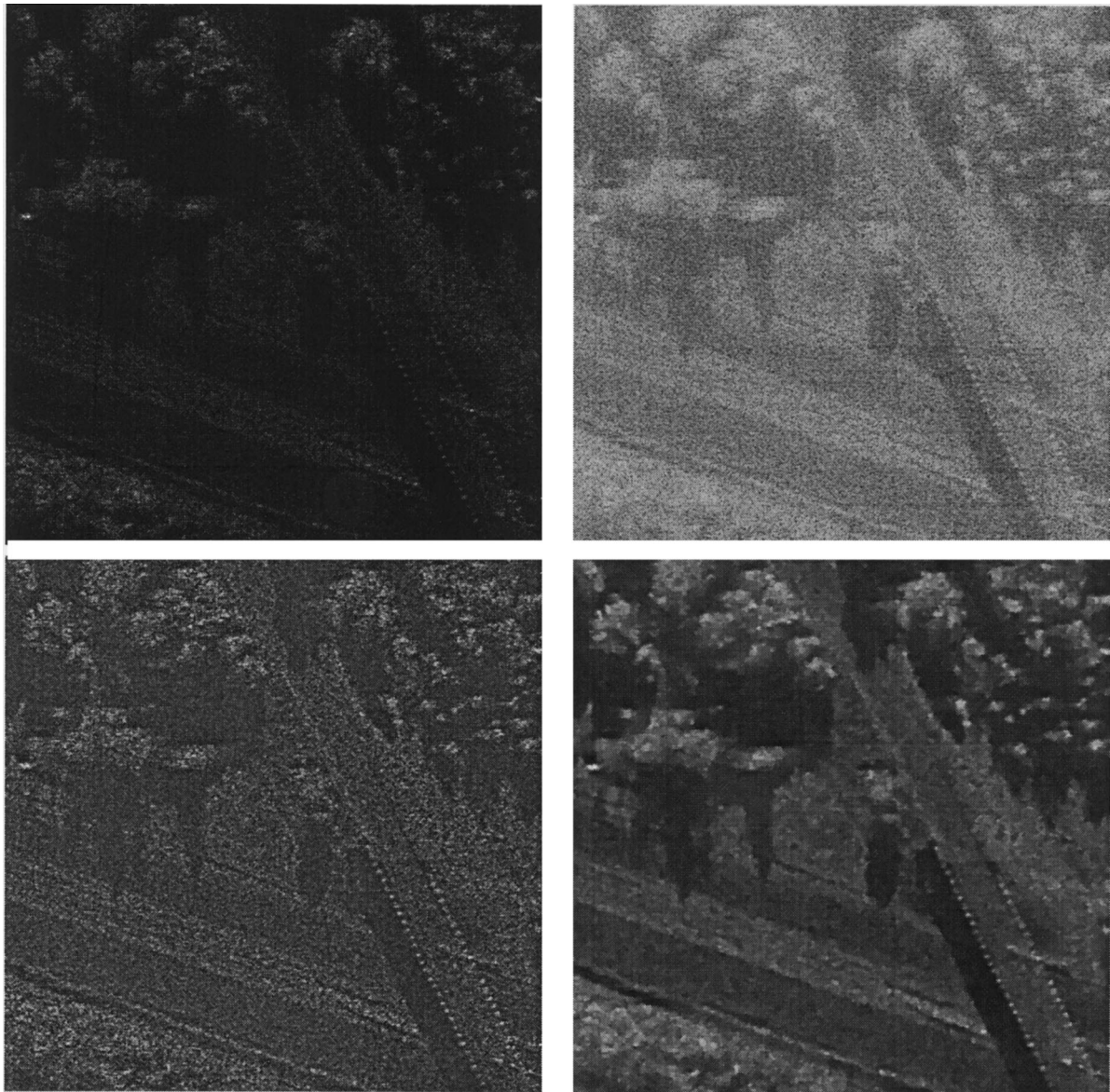


Fig. 1. (a) Top left: Unprocessed SAR image of upstate New York scene consisting of highway with bridge overpass. (b) Top right: Logarithm-transformed SAR image. (c) Bottom left: Stage 1 result averaged across spatial scales. (d) Bottom right: New BCS/FCS multi-scale enhancement.

regularizing, and completing boundaries degraded by sensor noise. Like the Grossberg et al. (1995) algorithm, the present one can be run independently at multiple scales, meaning that boundary signals are detected and completed, and surface representations filled-in, at small, medium and large scales, before a final composite is achieved by averaging. Compared with the Grossberg et al. (1995) version, the present multi-scale algorithm yields more efficient boundary processing, speeding run-time by a factor of approximately three. As shown in a subsequent section, moreover, long-range boundary completion, the rate-limiting factor for many possible implementation schemes, is sped-up by a factor of five. Furthermore, the current small-scale processing is so improved that it forms a useful image processing procedure in its own right, at a speed-up

of fifteen times compared to the older, multi-scale algorithm. The present algorithm is both closer in structure to known local circuits in the visual cortex (Grossberg et al., 1997; Ross et al., 1998) than the previous one, and simpler, containing fewer free parameters. Intuitions about its improved performance can best be appreciated by considering the model of visual cortical functioning upon which the algorithm is based. The Grossberg et al. (1997) model further develops the Boundary Contour System (BCS) model of Grossberg and Mingolla (1985a, b) by suggesting functional reasons for why the visual cortex is organized into layers, how these layers interact via local networks to form functional columns, and how these columns are embedded into cortical maps, to compute context-sensitive and coherent groupings of visual forms that preserve their

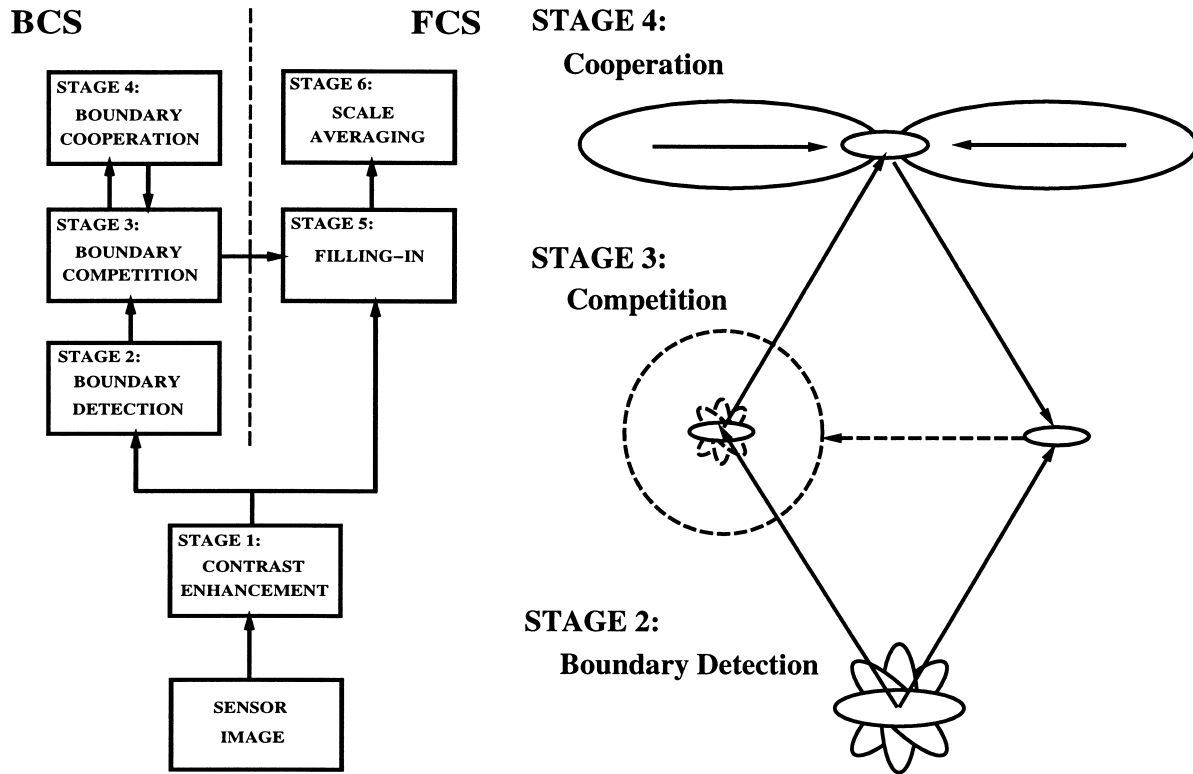


Fig. 2. A block diagram of the BCS/FCS system described in this article. Parallel boundary and feature processing streams interact to yield a structured smoothing that suppresses noise while enhancing surface contours. BCS processing occurs within a cooperative competitive feedback loop.

contrast-sensitivity and spatial context-sensitivity. We interchangeably call this latter property *analog coherence* or *coherent energy*. Thus the present model attempts to capture coherent properties of visual cortical processing in an efficient boundary segmenter.

Boundaries form barriers to the diffusive filling-in of

surface lightness. The final displayed lightness of a surface is determined in the model through processing at multiple scales. Multi-scale processing enhances surfaces occurring at a range of image sizes. The results is an image in which multi-scale surface boundaries and features are sharpened and accentuated and noise is reduced (Fig. 1(d)).

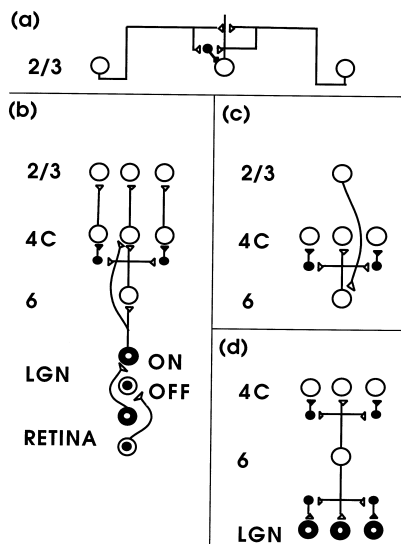


Fig. 3. Model retinal, lateral geniculate nucleus (LGN), and cortical V1 circuit (Reprinted with permission from Grossberg et al. (1997)).

2. The approach

Grossberg (1984) and Cohen and Grossberg (1984) introduced the Boundary Contour System (BCS) and Feature Contour System (FCS) models of boundary and surface processing. How the BCS and FCS fit into a comprehensive theory of biological and machine vision called Form-And-Color-And-Depth (FACADE) theory is discussed in Grossberg (1994). Grossberg and Mingolla (1985a, b, 1987) developed the BCS model to simulate how the visual system detects, completes, and sharpens boundary segmentations in response to a variety of stimuli. Our present work adapts a recent development of the BCS model which suggests how the laminar, columnar, and map organization of the visual cortex accomplishes boundary segmentation (Grossberg et al., 1997). For the purposes of image processing we have distilled this full biological model down to its functional essentials. This BCS/FCS system is diagrammed in Fig. 2.

The architecture in Fig. 2 incorporates three key design principles from Grossberg et al. (1997).

The first property concerns how the cortex achieves long-range cooperative completion or grouping by realizing a “bipole property”. This property refers to the disposition of certain cells in visual cortical areas V1 and V2 to fire in the presence of approximately aligned, but spatially separated, image gradients. According to the Grossberg et al. (1997) model, cooperative bipole interactions are achieved by excitatory long-range horizontal pathways among cortical pyramidal cells. In this section, these interactions will be considered only in the cortical area that is most directly activated by visual inputs, V1. In order for cooperation to build a boundary over gaps in an image, such as when collinear edge segments are interrupted by noise, these monosynaptic excitatory connections need to converge on shared pyramidal cells with collinear or slightly co-curved receptive fields (see Fig. 3(a)). The horizontal connections also activate smooth stellate cells, which inhibit nearby pyramidal cells via disynaptic inhibition (Hirsch and Gilbert, 1991; McGuire et al., 1991). Horizontal waves of activation resulting from spatially isolated inducers are attenuated rapidly by subsequent disynaptic inhibition. Locally, it is a case of one-against-one. Bipole completion occurs as a result of model interactions between monosynaptic excitation and disynaptic inhibition when layer 3 cells receive horizontally induced activations from a surrounding neighborhood of oriented cells, as in the middle of a contour. These activations from convergent horizontal connections can overcome the effect of disynaptic inhibition because all the horizontal connections are proposed to converge on a single population of saturating inhibitory interneurons (Fig. 3(a)). Locally, it is a case of two (or more) against one. The present model proposes an efficient computational approximation of this two-against-one principle that enables bipole cells to behave like statistical AND gates that act to complete and regularize image boundary representations.

The second design property suggests how inputs to V1 from the lateral geniculate nucleus or LGN (the way-station from the retina to V1) preserve their sensitivity to image contrasts (see Fig. 3(b)). As in the brain, LGN inputs to the cortex arrive with a concentric spatial competition (on-center, off-surround or off-center, on-surround) to activate orientationally tuned simple cells. The computation of oriented local image gradients for boundary detection is thus driven by a feedforward on-center off-surround network whose cells obey membrane equations, or shunting laws. Such a network preserves cell sensitivity to analog input values over a large dynamical range, while performing local normalization of image contrasts (Grossberg, 1973).

The third design property shows how the visual cortex makes double use of this competitive network to coherently select correct groupings, while suppressing incorrect ones, without a loss of analog sensitivity (see Fig. 3(c)). Earlier BCS/FCS algorithms exhibited a tendency for completed

boundary activations to saturate from the combination of positive feedback and the computations required to achieve the bipole property. In the present algorithm, the long-range cooperation of bipole units accesses the shorter-range on-center off-surround network that feeds simple cells. This amplifies those cell activations that are favored by the cooperative grouping, while suppressing those that are not, without compromising their sensitivity to image contrasts.

The BCS used herein consists of a series of boundary detection, competition, and cooperation stages as shown in the block diagram in Fig. 2. Stage 1 models the contrast enhancement resulting from on-center, off-surround (ON channel) and off-center, on-surround (OFF channel) interactions at the retina and LGN. These ON and OFF cells compensate for variable illumination by computing locally normalized contrast ratios throughout the image.

At Stage 2, these ON and OFF cells generate half-wave rectified outputs which together drive the activation of oriented simple cells. Simple cells compute a measure of the local image gradient magnitude and orientation, and this stage of BCS processing is similar to a number of classical procedures (Canny, 1986). Like-oriented simple cells sensitive to opposite contrast polarities or directions-of-contrast pool their activations at complex cells. Complex cells are hereby rendered insensitive to direction-of-contrast (dark-to-light vs. light-to-dark), as are all subsequent BCS processing stages.

Next, complex cell activations compete at Stage 3 processing. Competition occurs through on-center off-surround processing across both image space (spatial competition) and across orientation space (orientational competition). Spatial and orientational competition captures the functional implications of lateral inhibition across a cortical map in which nearby cells tend to be sensitive both to contrasts at neighboring (or overlapping) image locations and similar boundary orientations. Functionally, competition sharpens boundary localization and orientational tuning of individual complex cell filters. It also endows the complex cells with a property of *endstopping* that enables them to respond more vigorously near the end of a line than at its middle. This competition is also driven by feedback from Stage 4 long-range boundary cooperation, thereby suppressing weaker boundary activations while enhancing the contrast and the completion of stronger and more globally consistent boundary activations.

Long-range boundary cooperation at Stage 4 accomplishes the grouping together of consistent boundaries and the completion of camouflaged boundaries. This cooperation is achieved by bipole cells which realize a type of statistical AND gate, as they fire if both halves of their receptive fields are sufficiently activated by appropriately oriented input contrasts from the complex cells of Stage 3.

The cooperative–competitive (CC) feedback loop between Stage 3 and Stage 4 acts to complete and enhance spatially and orientationally consistent boundary groupings while inhibiting inconsistent ones. This feedback process

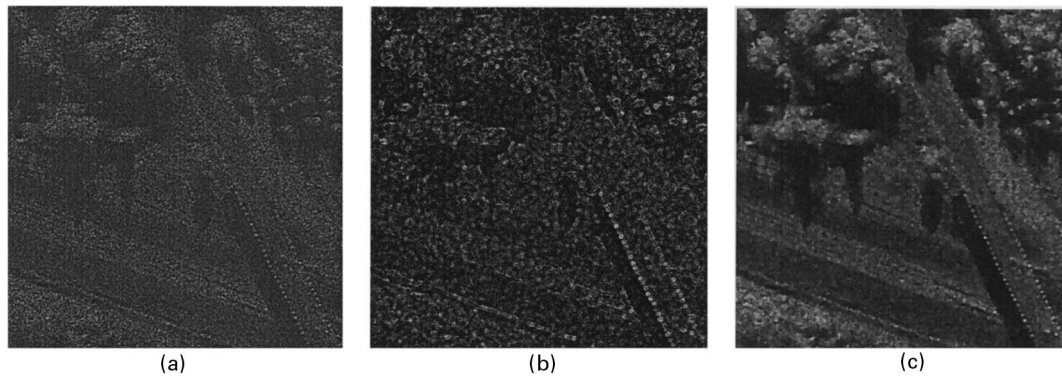


Fig. 4. (a) Stage 1: Normalized contrast enhancement. (b) Stage 3: BCS boundaries. (c) Stage 5: Diffused FCS surface representation.

simultaneously achieves the addition of sharp completions and the suppression of noise. Furthermore, excitatory and inhibitory feedback are balanced such that boundary strength sensitivity is preserved and boundary activations are not driven to saturation. The robust preservation of sensitivity to the analog strength of inputs that support long-range completion of boundary signals over gaps in the image—that is, regions of the image where local image data would not signal a boundary—is an important innovation of the present algorithm. Previous versions of the BCS tended to sacrifice sensitivity to input strength as a cost of the advantages of context-sensitive long-range grouping in a feedback system. The present architecture combines the nonlinear choice properties necessary to determine whether and where to coherently link boundary segments with sensitivity to input contrast magnitudes in the completed boundary signals.

The improved BCS boundaries act as barriers to diffusion of the ON and OFF contrast signals within the FCS. Fig. 4 shows how these processes act on a SAR image of a bridge crossing a highway in a wooded area of upper New York state. Dr. Allen Waxman of the Machine Intelligence Group at MIT Lincoln Laboratory kindly made these SAR images available to us.

Cohen and Grossberg (1984) and Grossberg and Todorović (1988) developed the FCS model to simulate data about human brightness perception. The combination of BCS boundary completion and FCS surface diffusion mechanism is an early exemplar of a class of image processing procedures known as anisotropic or geometry-driven diffusion. (See Fischl and Schwartz (1997) for a recent review.) Unlike most such approaches, however, BCS/FCS algorithms do not require that diffusion rates be limited by initial image data, or by iterative updates of any transformations of image data that are influenced by diffusion. Instead, the boundary signals that limit diffusion are computed by a self-equilibrating process that is both buffered from the effects of the diffusion process and capable of generating barriers to diffusion that are based on contextual image data at some distance from a pixel location, rather than simply on local measures of image gradients.

3. Image enhancement methods and results

The SAR images were obtained using a 35-GHz radar with 1 ft \times 1 ft resolution and slant range of 7 km (Novak et al., 1990). Fig. 1(a) shows a SAR image, Fig. 1(b) the image logarithmically transformed for viewing, Fig. 1(c) the summed ON – OFF contrast signals of our multi-scale system, and Fig. 1(d) the multi-scale BCS/FCS enhanced image.

BCS/FCS processing can be performed at multiple spatial scales to enhance object and surface features of various sizes. Figs. 5 and 6 show the FCS output for the bridge image of Fig. 4 processed at multiple scales. Image enhancement is significant in the small scale result shown in Fig. 6. However, certain features such as the bridge and the highway are more evident at the largest scale. These scales might prove useful in other image contexts or for recognition of large objects or surfaces. The multiscale combination in Fig. 5(f) shows both the high resolution of the small spatial scale and the smoothing of the larger spatial scales.

Fig. 6 illustrates the performance of both the BCS and the FCS at different scales. Comparison of the top row of Stage 2 complex cell activations with the middle row of Stage 3 boundary activations indicates how boundary salience is influenced by bipole grouping. Fig. 7 shows the new and old BCS systems, respectively, on a portion of the image including a stretch of the bridge overpass. The impact of this boundary processing for image enhancement is evident in Fig. 8 which shows a filled-in image bounded by small-scale Stage 2 complex cell responses next to a filled-in image bounded by small-scale Stage 3 boundaries.

3.1. Comparison to prior systems

The earlier BCS/FCS system that is illustrated in Fig. 7 (left) already offered improved image enhancement over iterative smoothing techniques, including the median filter (Scollar et al., 1984), adaptive averaging using the sigma filter (Lee, 1983), and geometric filtering (Crimmins,

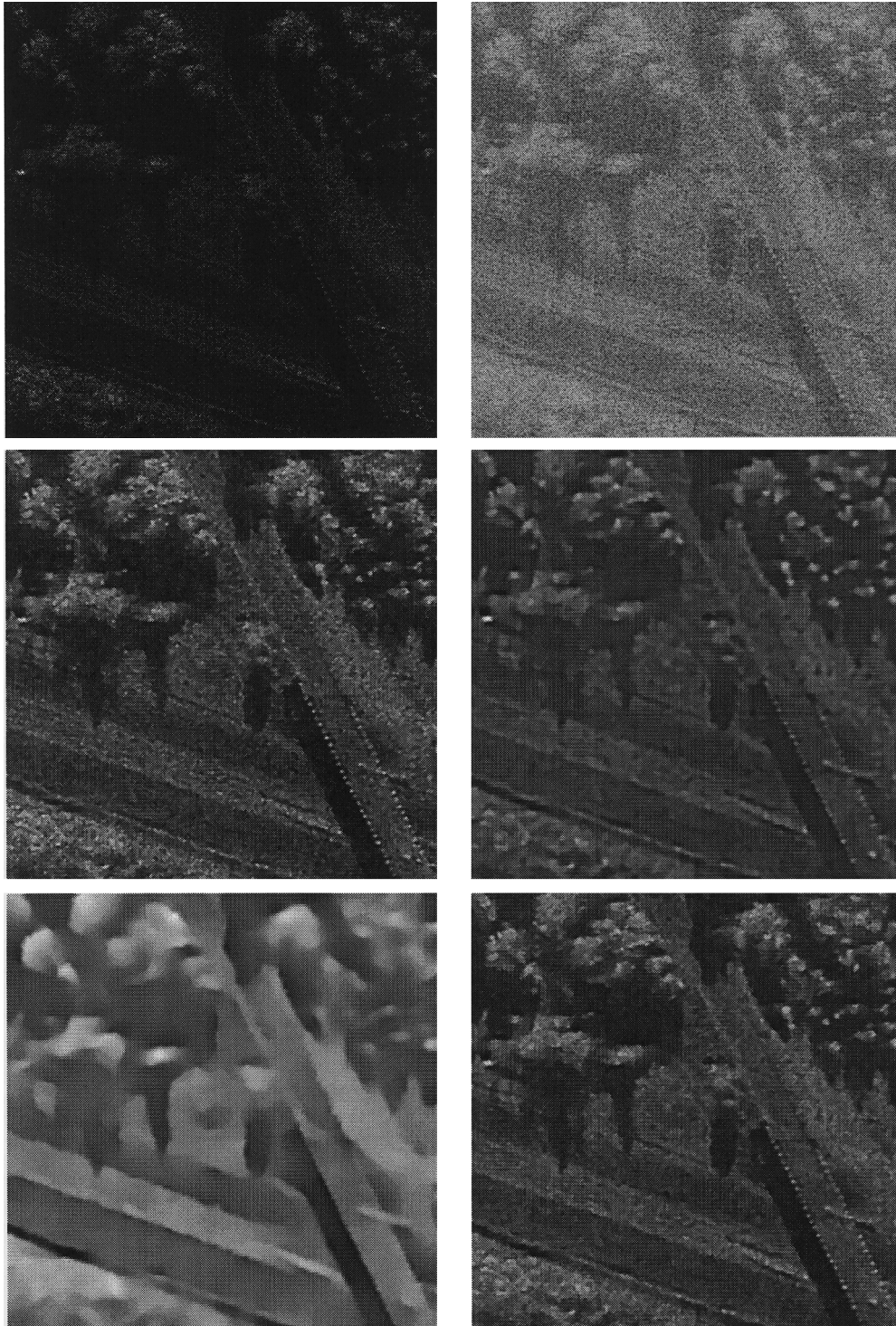


Fig. 5. Multiple scale surface processing: (a) Top left: Original image. (b) Top right: Log-compressed image. (c) Middle left: New BCS/FCS small-scale result. (d) Middle right: Medium-scale result. (e) Bottom left: Large-scale result. (f) Bottom right: Multi-scale result.

1985) This BCS/FCS system offered improved image enhancement over the results of these systems iterated for an optimal number of times. The BCS/FCS enhancement offers the further advantage that it converges upon a stable image appearance which is not degraded by continued

iteration, as occurs using the standard iterative techniques. Fig. 9 demonstrates that our new system also outperforms these standard statistical image enhancement techniques. To allow comparison, the statistical techniques were run on a nonlinear compression of the bridge overpass image

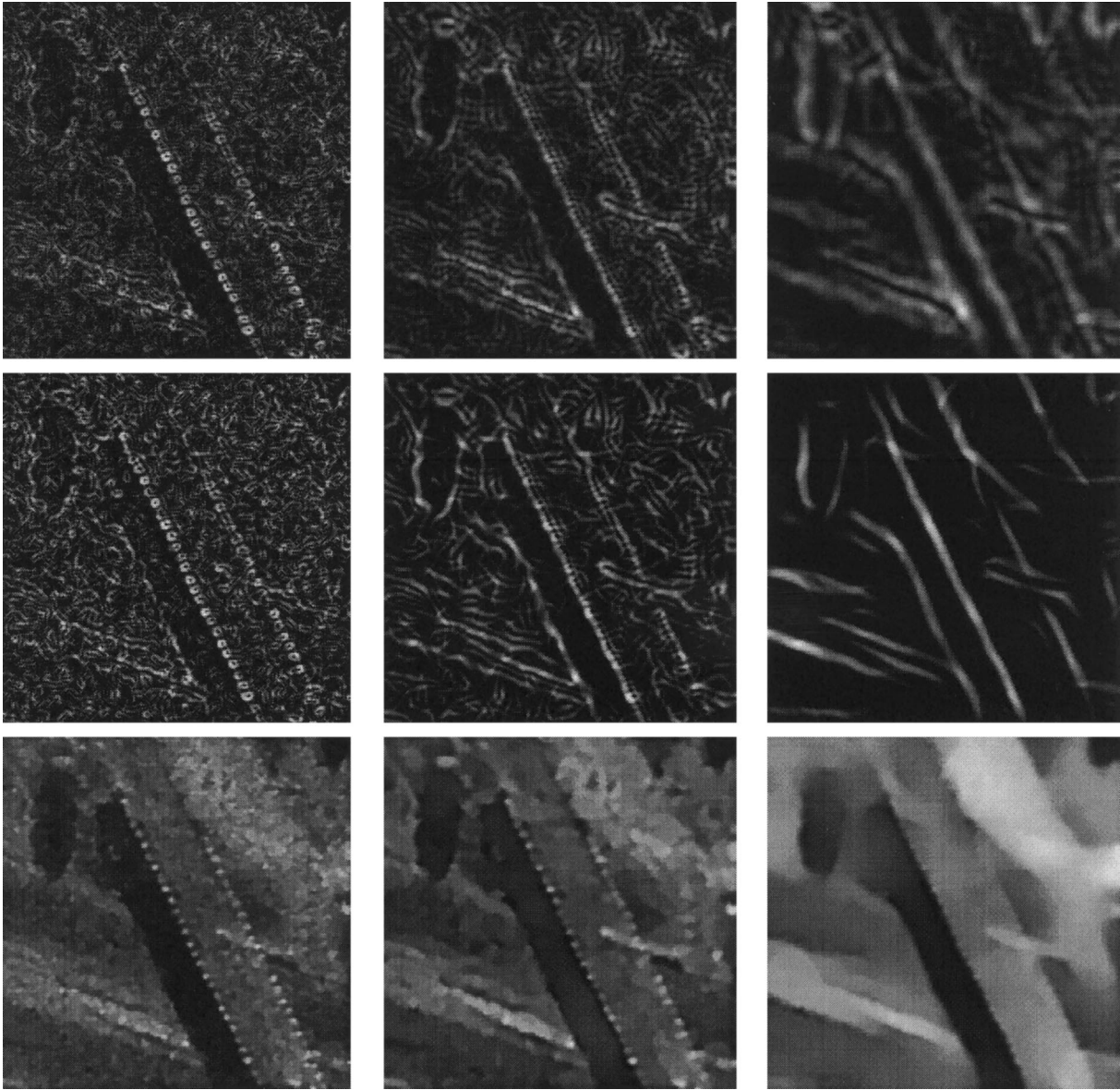


Fig. 6. Multiple scale boundary and surface processing: Top Row: Complex cell processing. Middle Row: Completed boundary activities. Bottom Row: Surface filling-in within the completed boundaries.

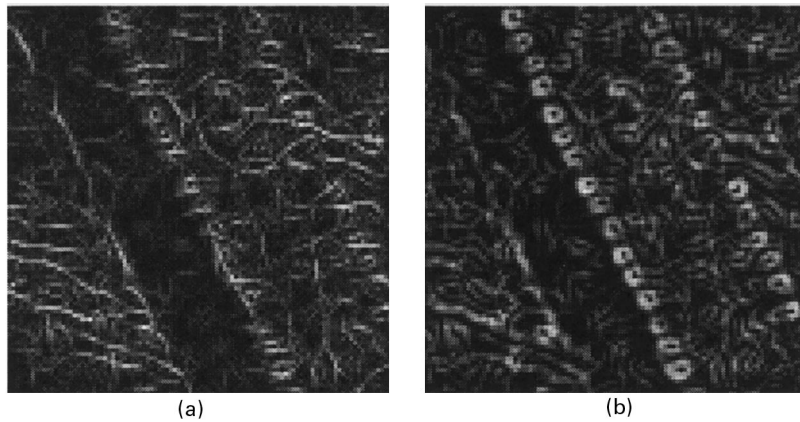


Fig. 7. The small scale boundary output of the BCS of Grossberg et al. (1995) is on the left. The improved algorithm's small-scale boundary output is on the right.

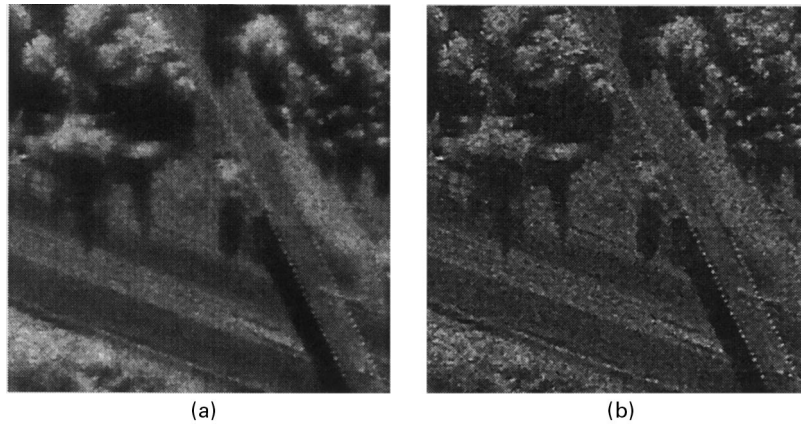


Fig. 8. Comparison of filling-in within (a) Stage 2 complex cell boundaries and (b) Stage 3 bipole-completed boundaries.

given by:

$$F(I) = \frac{I}{A + I}, \quad (1)$$

where A = the mean pixel intensity of 870 for the original bridge image data. The effect of this transformation is to produce input of roughly the same grayscale distribution as the BCS/FCS Stage 1 output. Parameters for each of these methods were set to smooth speckle noise as closely as

possible to the degree achieved by BCS/FCS processing, as determined by informal observation. The previous and present BCS/FCS systems are more complex than these statistical algorithms. This complexity translates to an increased amount of processing time and memory required and entails a more complex process of finding optimal parameters. BCS/FCS VLSI chips are currently being developed to offset these complexities (Waskiewicz et al., 1997).

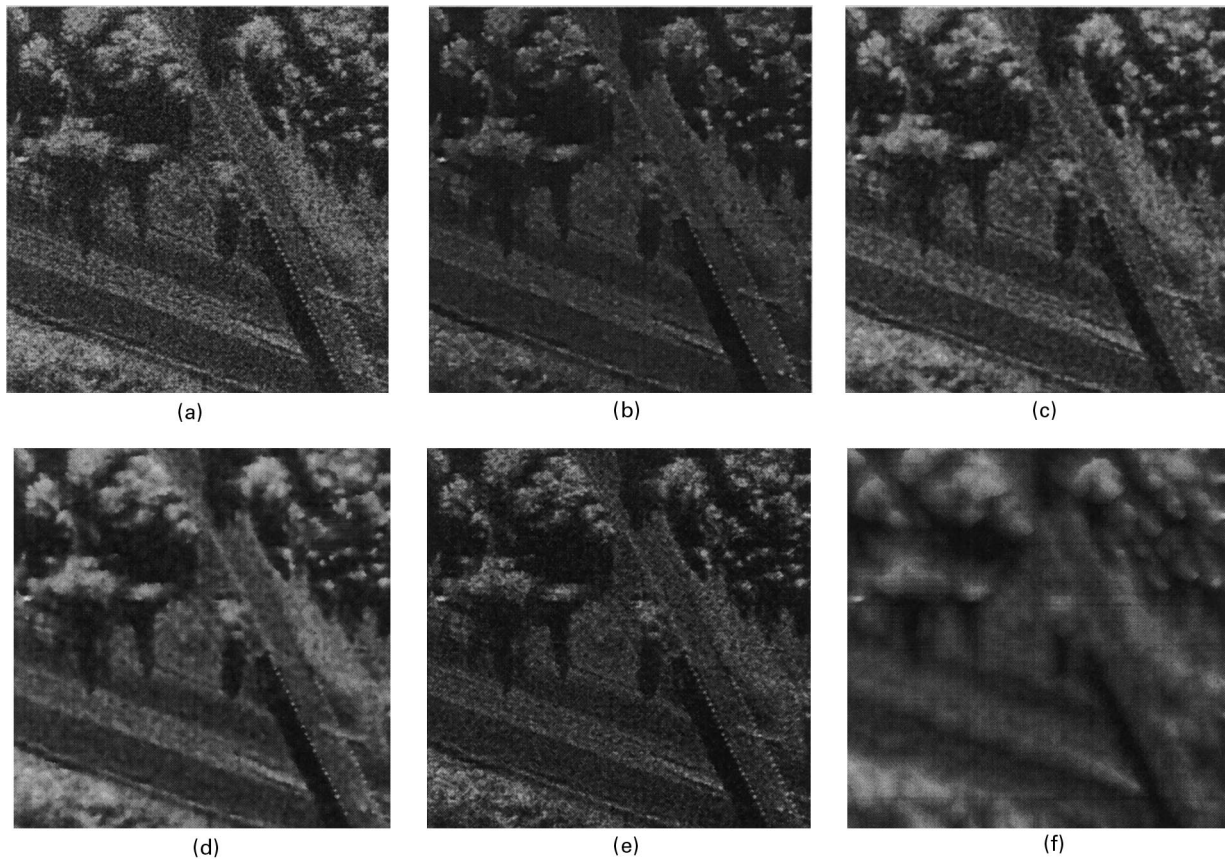


Fig. 9. (a) Input image with pixel values log-compressed for viewing; (b) Multi-scale new BCS/FCS result; (c) Output of three iterations of a 3×3 median filter; (d) Output of a 5×5 sigma filter (Lee, 1983); (e) Output of three iterations of a geometric filter (Crimmins, 1985); (f) Output of four iterations of a geometric filter.

Table 1
System parameters for BCS/FCS simulations

BCS/FCS Parameters			
Name	Description	Value	Equation(s)
Stage 1: ON and OFF			
Center-Surround Processing			
A	Activation decay rate	2000	6,7
D^+	ON Baseline activity	0.5	6
D^-	OFF Baseline activity	1.0	7
σ_c	Center size	0.3	8
σ_{s0}	Small surround size	1.2	9
σ_{s1}	Medium surround size	3.6	9
σ_{s2}	Large surround size	10.8	9
Stage2: Simple/Complex Boundary Detection			
σ_{v0}	Small simple cell width	0.75	15
σ_{v1}	Medium simple cell width	1.5	15
σ_{v2}	Large simple cell width	3.0	15
σ_{hg}	Simple cell length	$3\sigma_{v2}$	14
Stage 3: Competition			
A	Activation decay rate	30	17
B	Saturation level	10	17
C	Hyperpolarization level	0.5	17
G_f	Feedforward gain	0.25	18
G_b	Feedback gain	1.0	18
σ_{y0}	Small spatial surround size	4.0	19
σ_{y1}	Medium spatial surround size	8.0	19
σ_{y2}	Large spatial surround size	16.0	19
σ_k	Orientalional surround size	45°	19
Stage 4: Cooperation			
A	Activation decay rate	30	20
B	Saturation level	10	20
α	Nonlinearity constant	0.0000001	22
T	Bipole rule threshold	2.0	22
C_{l0}	Bipole length	8.0	23,24
C_{l1}	Bipole length	16.0	23,24
C_{l2}	Bipole length	32.0	23,24
C_{wg}	Bipole width	$0.5C_{lg}$	23,24
β	Distance blur	0.8	25
μ	Curvature blur	11	25
λ	Orientalional blur	90	25
Stage 5: Surface Filling-In			
D	Activation decay rate	1	25
δ	Permeability numerator factor	1	29
ϵ	Permeability denominator factor	2000	29

4. Model equations

Throughout this system, image arrays of neural units, or nodes, with activities u_{ij} , where i and j denote the position relative to the image array, combine excitatory E_{ij} and inhibitor I_{ij} inputs within an on-center (excitatory) off-surround (inhibitory) shunting equation (Grossberg, 1973):

$$\frac{du_{ij}}{dt} = -A(u_{ij} - D) + (B - u_{ij})E_{ij} - (C + u_{ij})I_{ij}, \quad (2)$$

with an excitatory on-center

$$E_{ij} = \sum_{p,q} \frac{1}{2\pi\sigma_E} \exp\left[-\frac{1}{2\sigma_E}((p-i)^2 + (q-j)^2)\right] F_{pq} \quad (3)$$

and an inhibitory off-surround

$$I_{ij} = \sum_{p,q} \frac{1}{2\pi\sigma_I} \exp\left[-\frac{1}{2\sigma_I}((p-i)^2 + (q-j)^2)\right] G_{pq}. \quad (4)$$

At equilibrium, each node's activity can be expressed as a biased Difference-of-Gaussians (DOG) divided by a biased Sum-of-Gaussians (SOG):

$$u_{ij} = \frac{AD + BE_{ij} - CI_{ij}}{A + E_{ij} + I_{ij}}. \quad (5)$$

The output $U_{ij} = [u_{ij}]^+$, where $[w]^+ = \max(w, 0)$, half-wave rectifies the activity u_i .

4.1. Stage 1. Contrast enhancement

The first processing stage performs a local contrast enhancement and normalization of image intensities. This is achieved through two shunting center-surround networks. An on-center off-surround network and an off-center on-surround network correspond to the ON and OFF channels, respectively, in the visual pathway. The two networks differ in the sign of their responses such that the ON channel shows enhanced response to image locations of high intensity relative to their surrounding image locations and the OFF channel shows enhanced response to image locations of low intensity relative to their surrounding image locations. Thus at equilibrium, the shunting equations for the ON and OFF networks achieve contrast-enhanced and normalized responses to the input sensor image S :

ON Cell Activation

$$X_{ij}^{g+} = \left[\frac{AD^+ + S_{ij}^c - S_{ij}^{sg}}{A + S_{ij}^c + S_{ij}^{sg}} \right]^+ \quad (6)$$

OFF Cell Activation

$$X_{ij}^{g-} = \left[\frac{AD^- + S_{ij}^s - S_{ij}^{sg}}{A + S_{ij}^s + S_{ij}^{sg}} \right]^+ \quad (7)$$

where

$$S_{ij}^c = \sum_{pq} S_{i+p,j+q} G_{pq}^c \quad \text{and} \quad S_{ij}^{sg} = \sum_{pq} S_{i+p,j+q} G_{pq}^{sg}, \quad (8)$$

and the weighting functions are defined by normalized Gaussians for the center (G^c) and surround (G^{sg}) connectivity, as in

$$G_{pq}^d = \frac{1}{\sigma_d \sqrt{2\pi}} \exp\left(-\frac{p^2 + q^2}{2\sigma_d^2}\right). \quad (9)$$

The ON and OFF networks have a baseline level of activation determined by D^+ in (6) and D^- in (7), respectively (Grossberg and Wyse, 1991). ON and OFF networks are applied at three spatial scales using the same center connectivity kernel with standard deviation σ_c for each, and three surround connectivity kernels of increasing standard deviations σ_{sg} , $g = 0, 1, 2$. (See Table 1.) For a discussion of the merits of this contrast-enhancement and normalization scheme relative to other related approaches, see Grossberg et al. (1995).

4.2. Stage 2. Boundary detection

At the second stage, oriented contrast is detected by nodes with connectivity analogous to that of cortical simple cells. Both ON and OFF network activity is used to gauge oriented contrast at each image location. An edge elicits a strong ON response next to a strong OFF response, an optimal coincidence for these boundary detectors. However, these detectors are not merely edge detectors. They also show weaker response to gradients of image texture or shading.

In particular, oriented arrays of spatially displaced ON and OFF cell inputs compete at each location with oppositely polarized OFF and ON arrays with the same orientation, before the net activity is half-wave rectified to generate output signals. As a result, simple cell receptive fields that receive uniformly distributed inputs generate zero outputs. Simple cell outputs at scale g , position (i, j) , and orientation k ($k = 0, 1, \dots, 11$) are thus modeled by the equations

$$s_{ijk}^{Rg} = \left[\left(R_{ijk}^{g+} + L_{ijk}^{g-} \right) - \left(R_{ijk}^{g-} + L_{ijk}^{g+} \right) \right]^+, \quad (10)$$

$$s_{ijk}^{Lg} = \left[-\left(R_{ijk}^{g+} + L_{ijk}^{g-} \right) + \left(R_{ijk}^{g-} + L_{ijk}^{g+} \right) \right]^+, \quad (11)$$

where

$$R_{ij}^{g+} = \sum_{pq} X_{pq}^{g+} G_{p,q+\sigma_{vg}/2,k}^g \quad \text{and} \quad (12)$$

$$R_{ij}^{g-} = \sum_{pq} X_{pq}^{g-} G_{p,q+\sigma_{vg}/2,k}^g,$$

$$L_{ij}^{g+} = \sum_{pq} X_{pq}^{g+} G_{p,q-\sigma_{vg}/2,k}^g \quad \text{and} \quad (13)$$

$$L_{ij}^{g-} = \sum_{pq} X_{pq}^{g-} G_{p,q-\sigma_{vg}/2,k}^g,$$

and

$$G_{p,q,k}^g = \frac{1}{2\pi\sigma_{hg}\sigma_{vg}} \exp\left(-\frac{1}{2}\left(\frac{p\cos(\pi k/12) - q\sin(\pi k/12)}{\sigma_{hg}}\right)^2 - \frac{1}{2}\left(\frac{p\cos(\pi k/12) + q\sin(\pi k/12)}{\sigma_{vg}}\right)^2\right). \quad (14)$$

The use of ON and OFF cells to form boundaries overcomes complementary deficiencies of each detector in responding to changing contour curvatures and to dark or light noise pixels (cf., Carpenter et al., 1989; Grossberg and Todorović, 1988). Simple cell outputs of the same orientation with opposite contrast polarities then are pooled to yield a contrast polarity-insensitive complex cell response:

$$c_{ijk}^g = s_{ijk}^{Lg} + s_{ijk}^{Rg}. \quad (15)$$

4.3. Stage 3. Boundary competition

Detected boundaries are passed into the cooperative-competitive loop, which includes Stages 3 and 4 of Fig. 2. This nonlinear feedback network groups, completes, and sharpens globally consistent boundary positions and orientations while suppressing weaker and redundant boundary activations. Competition between boundary activations occurs across both space and orientation, reflecting the functionality of spatially localized inhibition across the topography of visual cortex in which the variables of space and orientation are interwoven in a single spatial

map. Competition is driven by both bottom-up activation from boundary detection cells and top-down activation from boundary cooperation cells, allowing global groupings to effect local decisions. This BCS implementation involves fewer loop stages than previous versions of the BCS. Now a closer interaction of cooperative and competitive processes achieves better spatial context-sensitivity, contour strength sensitivity, and decision-making speed. As a result, only two iterations of this two-stage loop achieve performance which compares favorably with previous implementations run for several more iterations.

The boundary competition process obeys the equations:

$$Y_{ij}^g = \left[\frac{BE_{ij}^{3g} - CI_{ij}^{3g}}{A + E_{ij}^{3g} + I_{ij}^{3g}} \right]^+, \quad (16)$$

where

$$E_{ij}^{3g} = G_f c_{ijk}^g + G_b Z_{ijk}^g. \quad (17)$$

In (17), c_{ijk}^g represents bottom-up complex cell activation from (15), Z_{ijk}^g is the feedback contribution from Stage 4 cooperative boundary signals, and G_f and G_b are feedforward and feedback gain contrasts, respectively. In (16):

$$I_{ij}^{3g} = \sum_{mno} E_{i+m,j+n,k+o}^{3g} G_{mno}^{yg}. \quad (18)$$

Gaussians G_{mno}^{yg} in (18) obey (14) and exist at three scales, $g = 0, 1, 2$. The spatial standard deviations or blurring constants for each are given in the Stage 3 section of Table 1 as $\sigma_{y0}, \sigma_{y1}, \sigma_{y2}$. The orientational standard deviation for all of these scales is given by σ_k .

4.4. Stage 4. Boundary cooperation

The boundary cooperation, or bipole cells, are designated to generate outputs if suitably oriented inputs from the Stage 3 competition are active on both sides of its cell body. Thus, bipole cells generate the following steady-state outputs:

$$Z_{ij}^g = \left[\frac{BE_{ij}^{4g}}{A + E_{ij}^{4g}} \right]^+, \quad (19)$$

where

$$E_{ij}^{4g} = Y_{ijk}^g + H_{ijk}^{4g}, \quad (20)$$

and

$$H_{ijk}^{4g} = \left[f(h_{ijk}^{rg}) + f(h_{ijk}^{lg}) + h_{ijk}^{rg} + h_{ijk}^{lg} - T \right]^+. \quad (21)$$

In (21), h^{rg} and h^{lg} are the convolutions of Z with the right and left halves of a bipole kernel z (defined later), and $f(w) = (w)/(\alpha + w)$ where α is very small. Eq. (21) works by having the first two terms rapidly saturate to a value close to 1.0 whenever a nonzero input is processed in each half of the bipole's input field, as defined by Eqs. (22) and (23) later. Setting $T = 2.0$ in (21) then guarantees that the bipole cell will exceed threshold only if inputs arrive to both sides

because the values of h_{ijk}^{rg} and h_{ijk}^{lg} are themselves bounded between 0.0 and 1.0, owing to the choices of constants defining minimum and maximum attainable values for system variables through Stage 3; namely:

$$h_{ijk}^{rg} = \sum_{mno} Z_{i+m,j+n,k+o}^g \left[z_{2m/C_{lg}, 2n/C_{wg}, o, k} \right]^+, \quad (22)$$

with $m \geq 0$ and $n \geq 0$, and

$$h_{ijk}^{lg} = \sum_{mno} Z_{i+m,j+n,k+o}^g \left[-z_{2m/C_{lg}, 2n/C_{wg}, o, k} \right]^+, \quad (23)$$

with $m \leq 0$ and $n \leq 0$, where

$$z_{mno}^g = \text{sgn}\{m\} \exp\{-\beta(m^2 + n^2)\} \exp\{-\mu(n/m^2)^2\} \\ \times \cos^\lambda\{(k - o)\pi/K - \text{sgn}\{m\} \arctan(2n/m, m)\}. \quad (24)$$

The bipole kernel in Eq. (24) is composed of three parts which determine how the bipole filter values decrease as a function of the: (1) distance from the center of the filter: $\exp\{-\beta(m^2 + n^2)\}$; (2) spatial deviation from collinearity: $\exp\{-\mu(n/m^2)^2\}$; and (3) orientational deviation from collinearity: $\cos^\lambda\{(k - o)\pi/K - \text{sgn}\{m\} \arctan(2n/m, m)\}$. The cooperative–competitive loop is run independently at three different scales, with bipole filters defined by Eq. (24) at filter sizes C_{lg} and C_{wg} ($l = \text{length}$, $w = \text{width}$), $g = 0, 1, 2$, given in Table 1.

4.5. Stage 5. Surface filling-in

The BCS produces boundary signals that act as barriers to diffusion within the FCS. BCS signals from Stage 3 are used to gate diffusion within the filling-in domains of Stage 5 that are activated by the normalized ON and OFF cell outputs from Stage 1. For image pixels through which no boundary signals pass, resulting intensity values become more homogeneous as the diffusion evolves. Where boundary signals intervene, however, they inhibit diffusion, leaving a resulting activity difference on either side of the boundary signal. Thus, the boundaries serve as a structure-sensitive mesh, called a *boundary web*, which tracks the statistics of edges, textures, and shading, while smoothing over statistically irrelevant noise.

There are ON and OFF filling-in domains corresponding to the Stage 1 ON and OFF cells:

ON Filling-In

$$\frac{dF_{ij}^{g+}}{dt} = -DF_{ij}^{g+} + \sum_{p,q \in N_{ij}} (F_{pq}^{g+} - F_{ij}^{g+}) P_{pqij}^g + X_{ij}^{g+}, \quad (25)$$

where X_{ij}^{g+} is the Stage 1 ON cell output.

OFF Filling-In

$$\frac{dF_{ij}^{g-}}{dt} = -DF_{ij}^{g-} + \sum_{p,q \in N_{ij}} (F_{pq}^{g-} - F_{ij}^{g-}) P_{pqij}^g + X_{ij}^{g-}, \quad (26)$$

where X_{ij}^{g-} is the Stage 1 OFF cell output. At equilibrium,

$$F_{ij}^{g+} = \frac{X_{ij}^{g+} + \sum_{p,q \in N_{ij}} F_{pq}^{g+} P_{pqij}^g}{D + \sum_{p,q \in N_{ij}} P_{pqij}^g}, \quad (27)$$

and

$$F_{ij}^{g-} = \frac{X_{ij}^{g-} + \sum_{p,q \in N_{ij}} F_{pq}^{g-} P_{pqij}^g}{D + \sum_{p,q \in N_{ij}} P_{pqij}^g}. \quad (28)$$

The boundary-gated permeabilities in (27) and (28) obey

$$P_{pqij}^g = \frac{\delta}{1 + \varepsilon(y_{pq}^g + y_{ij}^g)}, \quad (29)$$

where

$$y_{ij}^g = \sum_k Y_{ijk}^g. \quad (30)$$

Eq. (29) shows how strong boundary signals decrease permeability and thereby bound each filling-in domain. In our simulations, the diffusion of image features was accomplished by iteratively solving for “new” values (left side of Eqs. (27) and (28)) using current values (right sides of equations) for 800 iterations, to ensure a good approximation to equilibrium.

4.6. Stage 6. Scale averaging

At this final stage, equilibrated filled-in surface activities are combined between ON and OFF channels and across scale. A simple linear combination rule yields favorable results, based on informal observations:

$$M_{ij} = 4(F_{ij}^{0+} - F_{ij}^{0-}) + 2(F_{ij}^{1+} - F_{ij}^{1-}) + (F_{ij}^{2+} - F_{ij}^{2-}). \quad (31)$$

5. Discussion

The major improvements of the present algorithm over that of Grossberg et al. (1995) can best be appreciated by considering Stage 3 of the earlier algorithm, which includes complex cell output at 12 orientations, computed at three scales. That stage of complex cells occurred in a feed-forward “front-end” of the algorithm, that then sent signals to a cooperative–competitive feedback loop, which included five separate stages for boundary completion and regularization. The present algorithm was inspired by our recent model of the laminar circuitry for perceptual grouping in cortical areas V1 and V2 (Grossberg et al., 1997). It is a faster system with fewer parameters and less corruption of fine-scale boundary signals, achieved by employing closer interaction between bottom-up activation, short-range competition, and long-range cooperation than the earlier

algorithm. For example, in the current algorithm, bottom-up and top-down on-center and off-surround impact the same cells in Stage 3, instead of being computed separately. This allows the signals generated by long-range cooperative grouping for boundary completion to more robustly maintain analog sensitivity to the strength of the bottom-up signals that support completion, and thus to generate more appropriate groupings.

The boundary signals of the present system are not driven to saturation because the input to the bipoles are under the control of a negative feedback loop (short-range competition). Completed signals are, however, “lifted out” out of the “noise” of boundary signals that do not form coherent groupings. The improvement offered by this better integration of local and long-range contextual information is shown in the enlarged image of fine-scale boundaries on and near the bridge (Fig. 7).

More efficient processing has been achieved through a reduction in the total number of stages from nine to six, a reduction in the number of necessary iterations of the cooperative–competitive loop from five to two, and a computational speedup that is conservatively estimated to be by a factor of three.

Acknowledgements

EM was supported in part by the Defense Advanced Research Projects Agency and the Office of Naval Research (ONR N00014-95-1-0409) and the Office of Naval Research (ONR N00014-94-1-0597). WR was supported in part by the Air Force Office of Scientific Research (AFOSR 90-0175), British Petroleum (BP 89A-1204), HNC Software Inc. (SC-94-001), the National Science Foundation (NSF IRI-90-00530), and the Office of Naval Research (ONR N00014-91-J-4100). SG was supported in part by the Defense Advanced Research Projects Agency and the Office of Naval Research (ONR N00014-95-1-0409), the National Science Foundation (NSF IRI-97-20333), and the Office of Naval Research (ONR N00014-95-1-0657). The authors wish to thank Cynthia E. Bradford for her assistance in the preparation of the manuscript, and Jim Williamson for helpful comments on an earlier draft.

References

- Canny, J. (1986). A computational approach to edge detection. *IEEE Transactions on Pattern Analysis and Machine Intelligence*, 8 (6), 679–698.
- Carpenter, G. A., Grossberg, S., & Meharian, C. (1989). Invariant recognition of cluttered scenes by a self-organizing ART architecture: CORT-X boundary segmentation. *Neural Networks*, 2, 169–181.
- Cohen, M. A., & Grossberg, S. (1984). Neural dynamics of brightness perception: Features, boundaries, diffusion, and resonance. *Perception and Psychophysics*, 36, 428–456.
- Crimmins, T. (1985). Geometric filter for speckle reduction. *Applied Optics*, 24, 1438–1443.

- Fischl, B., & Schwartz, E. (1997). Learning and integral equation approximation to nonlinear anisotropic diffusion in image processing. *IEEE Transactions on Pattern Analysis and Machine Vision*, 19 (4), 342–351.
- Grossberg, S. (1973). Contour enhancement, short term memory, and constancies in reverberating neural networks. *Studies in Applied Mathematics*, 52, 217–257.
- Grossberg, S. (1984). Outline of a theory of brightness, color, and form perception. In: E. Degreef & J. van Buggenhaut (Eds.), *Trends in mathematical psychology*. Amsterdam: North Holland.
- Grossberg, S. (1994). 3-D vision and figure-ground separation by visual cortex. *Perception and Psychophysics*, 55, 48–120.
- Grossberg, S., & Mingolla, E. (1985a). Neural dynamics of form perception: Boundary completion, illusory figures, and neon color spreading. *Psychological Review*, 92, 173–211.
- Grossberg, S., & Mingolla, E. (1985b). Neural dynamics of perceptual grouping: Textures, boundaries, and emergent segmentations. *Perception and Psychophysics*, 38, 141–171.
- Grossberg, S., & Mingolla, E. (1987). Neural dynamics of surface perception: Boundary webs, illuminants, and shape-from-shading. *Computer Vision, Graphics and Image Processing*, 37, 116–165.
- Grossberg, S., Mingolla, E., & Williamson, J. (1995). Synthetic aperture radar processing by a multiple scale neural system for boundary and surface representation. *Neural Networks*, 8, 1005–1028.
- Grossberg, S., Mingolla, E., & Ross, W. D. (1997). Visual brain and visual perception: How does the cortex do perceptual grouping? *Trends in Neurosciences*, 20, 106–111.
- Grossberg, S., & Todorović, D. (1988). Neural dynamics of 1-D and 2-D brightness perception: A unified model of classical and recent phenomena. *Perception and Psychophysics*, 43, 241–277.
- Grossberg, S., & Wyse, L. L. (1991). A neural network architecture for figure-ground separation of connected scenic figures. *Neural Networks*, 4, 723–742.
- Hirsch, J. A., & Gilbert, C. D. (1991). Synaptic physiology of horizontal connections in the cat visual cortex. *Journal of Neuroscience*, 11, 1800–1809.
- Lee, J. (1983). A simple speckle smoothing algorithm for synthetic aperture radar images. *IEEE Transactions on Systems, Man and Cybernetics*, SMC-13, 85–89.
- McGuire, B. A., Gilbert, C. D., Rivlin, P. K., & Wiesel, T. N. (1991). Targets of horizontal connections in macaque primary visual cortex. *Journal of Comparative Neurology*, 305, 370–392.
- Munsen Jr, D., O'Brien, J., & Jenkins, W. (1983). A tomographic formulation of spotlight-mode synthetic aperture radar. *Proceedings of the IEEE*, 71 (8), 917–925.
- Munsen Jr, D., & Visentin, R. L. (1989). A signal processing view of strip-mapping synthetic aperture radar. *IEEE Transactions on Acoustics, Speech and Signal Processing*, 37 (12), 2131–2147.
- Novak, L., Burl, M., Chaney, R., & Owirka, G. (1990). Optimal processing of polarimetric synthetic-aperture radar imagery. *The Lincoln Laboratory Journal*, 3 (2), 273–290.
- Ross, W.D., Grossberg, S., & Mingolla, E., 1998 Visual cortical mechanisms of perceptual grouping: Interacting layers, networks, columns, and maps (in preparation).
- Scollar, L., Weidner, B., & Huang, T. (1984). Image enhancement using the median and the interquartile distance, *Computer Vision, Graphics, and Image Processing*, 25, 236–251.
- Waskiewicz, J., Cauwenberghs, G., & Yochelson, D. (1997) Focal-plane analog VLSI implementation of the BCS image segmentation algorithm. *Proceedings of the 31st annual conference on information sciences and systems*. Baltimore, MD, March, pp. 341–344.